Journal of Polymer Science

WILEY

JOURNAL OF POLYMER SCIENCE

RESEARCH ARTICLE OPEN ACCESS

Influence of Poly(Diketopyrrolopyrrole) Chain Length and Chemical Structure on Photocatalytic Hydrogen Evolution in Composites With TiO_2

Teresa Mauerer[1] | Julian Hungenberg[2] | Mukundan Thelakkat[2,3] | Roland Marschall[1]

[1]Physical Chemistry III, University of Bayreuth, Bayreuth, Germany | [2]Applied Functional Polymers, University of Bayreuth, Bayreuth, Germany | [3]Bavarian Polymer Institute, University of Bayreuth, Bayreuth, Germany

Correspondence: Mukundan Thelakkat (mukundan.thelakkat@uni-bayreuth.de) | Roland Marschall (roland.marschall@uni-bayreuth.de)

Received: 13 February 2025 | **Revised:** 14 March 2025 | **Accepted:** 25 March 2025

Funding: This work was supported by Bayerisches Staatsministerium für Wissenschaft, Forschung und Kunsthttp, Solar Technologies Go Hybrid.

Keywords: heterojunction | hydrogen generation | photocatalysis | polymers

ABSTRACT

For this study, we have synthesized two different poly(diketopyrrolopyrrole) copolymers with different chain lengths. The diketopyrrolopyrrole (DPP) core is substituted with oligoethylene glycol side chains to increase its compatibility with water and copolymerized with either fluorene or carbazole moieties. The polymers form a composite photocatalyst with anatase TiO_2. Detailed characterization such as NMR spectroscopy, UV–Vis, DRIFT, and UPS is used to analyze the structural and optical properties as well as the frontier orbital energy levels of the components and the composite materials. The optical properties of the polymers are tunable with respect to the copolymer used, opening up the possibility of optimizing the photocatalytic activity. These composite materials (without the addition of a co-catalyst) provide up to an eightfold enhancement of the hydrogen evolution reaction (HER) compared to pristine TiO_2. The polymers also exhibit stability in the reaction medium as shown by solid-state NMR, DRIFT, and UV–Vis spectroscopy. A significant influence of the chain length of the polymers on HER is found as well. As the chain length increases, the activity toward hydrogen evolution increases. We show a correlation between hydrogen evolution and PDPP chain length whereby the active site of the photocatalytic process remains the inorganic semiconductor.

1 | Introduction

The apparent effects of climate change present a significant threat to humanity, as extreme weather, rising ocean levels, and increasing temperatures cause substantial disruptions to ecosystems, human health, and economies [1]. Therefore, it is essential to reduce greenhouse gas emissions and transition to renewable energy sources. Solar energy and hydrogen technologies are particularly promising in this regard [2]. In 1972, the photoelectrochemical water splitting to produce hydrogen from water at the surface of TiO_2 was reported by Fujishima and Honda [3]. Since then, a vast number of inorganic semiconductors have been investigated for this reaction, including oxides like, for example, $SrTiO_3$ [4–7], or ZnO [8, 9]. The primary limitation of these materials is their wide band gap, which restricts their use to only UV light.

In recent years, organic photocatalysts have emerged as promising candidates for the photocatalytic hydrogen evolution reaction (HER) [10–13]. The advantages of organic and polymeric semiconductors are particularly evident in their diverse synthetic modularity and, thus, the ability for chemical tailoring of electronic and photophysical properties, as well as shifting the absorption to visible light wavelengths. Additionally, these materials exhibit earth abundance and activity in hydrogen evolution without the need for noble metal co-catalysts.

In 2015, Sprick et al. published a report on the HER using organic polymer networks [14]. The same research group subsequently published a report on HER using linear conjugated polymers, with a particular focus on the homopolymer of dibenzo[*b,d*]thiophene sulfone, known as P10 [15]. Strategies to influence the band gap include extending the π-conjugation length and copolymerizing an electron-rich (donor, D) and an electron-poor unit (acceptor, A) in an alternating fashion [16, 17]. The alternation of an electron-pulling and pushing group leads to an enhanced delocalization of the π-electrons and the quinoid structure of the polymer. An increase in the quinoidal character of the polymer results in a reduction in the band gap [18, 19]. These modifications permit the utilization of visible light and enhance the efficiency under solar irradiation.

The donor and acceptor moieties can be intrinsically combined in the polymer structure to form a donor-acceptor copolymer, which may act as a donor or acceptor material depending on the D and A units. Alternatively, a bulk heterojunction (BHJ) of a donor and an acceptor polymer can be created by a physical combination (bilayer, blend, etc.) to form a heterojunction for photoinduced charge separation. BHJ comprising a benzodithiophene-based donor polymer coded as PBDTTTPD and a non-fullerene naphthalene diimide-based acceptor named PNDIHDT has been shown to result in a tandem cell for overall water splitting with a solar to hydrogen efficiency of 0.8% [20]. Furthermore, organic BHJ photocatalysts comprising a D/A heterojunction have been demonstrated to intrinsically dissociate excitons and enhance the charge carrier lifetime [21]. Despite this, they were found to be thermodynamically highly unstable and the quinoid form of the polymer was lost [22]. D-A copolymers are an effective strategy to overcome this issue.

On the other hand, the combination of both inorganic and organic semiconductors enables overcoming the limitations of, for example, TiO_2, such as low quantum yield and the lack of absorption in visible light [23]. This approach utilizes the distinctive attributes of both materials to augment their photocatalytic activity. The highest HER (300 W Xe lamp, $\lambda > 420$ nm) was achieved with a heterojunction between poly(benzothiadiazole) B-BT-1,4-E and TiO_2 and triethanolamine (TEOA) as sacrificial agent (SA), with a value of 220.4 μmol h^{-1} [24]. The effect of nano structuration in composite materials was reported with a phenylene vinylene conjugated porous polymer on TiO_2 named n-IEP-20@T-10 with eight times higher hydrogen evolution in comparison to the non-nanostructured [25]. The organic–inorganic heterojunction PB2T-TEG-TiO_{2-X} shows the facilitation of the ion uptake by the insertion of oligoethylene side chains. These side chains also enhance the interaction with TiO_{2-X}, leading to a 2.8 times increased HER in comparison to TiO_{2-X} [26].

Diketopyrrolopyrroles (DPP) can act as dye-sensitizing agents, thereby enhancing the photocatalytic activity. The Reisner group reported the synthesis of five DPP-sensitized photocatalysts, in which Co and Ni were identified as the active centers. The dyes and catalysts were immobilized with phosphonic acid on the surface of TiO_2 (P25). The dye-TiO_2-Ni//Co systems were demonstrated to be highly effective photocatalysts for the HER in ascorbic acid or TEOA aqueous solution [27]. Yang et al. reported the synthesis of a polydiketopyrrolopyrrol (PDPP) copolymerized with a carbazole comonomer. The carbazole's amino group was initially protected with *t-boc*. Following thermal treatment at 180°C, the protection group was removed, allowing the polar amino group to bind to the surface of TiO_2 and form a heterojunction interface. This cleaved heterojunction exhibited enhanced activity in the degradation of methyl orange in comparison to the uncleaved variant. Moreover, an elevated level of activity was observed for polymers with a higher molecular weight [28]. PDPPs are typically characterized by favorable charge carrier mobility, a relatively low optical band gap, and a high absorption coefficient [29–31]. Insertion of triethylene glycol side chains not only increases the hydrophilicity of the polymers [31–34], but also enhances the photocatalytic activity [35, 36].

Here, we report the synthesis and characterization of two PDPP copolymers with a donor-acceptor architecture and solubilizing side chains, as illustrated in Figure 1a. The DPP moiety acts as the acceptor unit and the thiophene unit and the comonomers fluorene and carbazole are the donor part. The D-A copolymers function as dye-sensitizing agents on TiO_2 to enhance the photocatalytic activity. Furthermore, the modification of polymer chain lengths was observed to result in a notable enhancement of the hydrogen evolution activity of these composite materials. The combination of the advantageous properties of PDPP polymers and TiO_2 allows for the effective utilization of visible light with sustainable photocatalysts for the hydrogen evolution reaction. A significant influence of the chain length of the polymers is found as well. As the chain length increases, the activity toward hydrogen evolution increases.

2 | Results and Discussion

2.1 | Polymers

The DPP core was synthesized according to a published protocol [31, 37]. It is flanked by two thiophene units $[T]_2$ and brominated at the fifth position of these thiophenes. At the N-position, the DPP core is modified with a triethylene glycol side chain (TEG), which increases the material's hydrophilicity [31]. The DPP core is copolymerized with either fluorene or carbazole donor units, resulting in the formation of a hole transport material. Both comonomers possess aliphatic side chains, which enhance solubility in organic solvents, and a pinacol borane as a functional unit for the Suzuki coupling. The Suzuki–Miyaura polycondensation reaction was conducted in toluene at 110°C using $Pd_2(dba)_3$ as the catalyst and K_2CO_3 as the base in sealed vials via thermal heating for 19 h. The protocol was then modified for a microwave synthesis. The temperature was increased to 140°C, and the reaction time was reduced to 2–3 h. All polymers were terminated with benzene units by using (4-bromophenyl)phosphonic acid. The phosphonic acid was added as a bridging unit between the polymer and the inorganic semiconductor. More synthetic details and the whole route are provided in the Figure S1. The microwave synthesis yielded between 18% and 35% of the desired product. The ^{1}H-NMR spectra are presented in Figures S2 and S3. Figure 1b illustrates the structures of the polymers, which are designated as PDPP$[T]_2${TEG}-Flu and PDPP$[T]_2${TEG}-Car. ^{31}P-NMR characterization regarding the successful application of (4-bromophenyl)phosphonic acid as an endcapper did not

show any signal (Figures S4 and S5). Therefore, bromobenzene was also used as an endcapper.

Gel permeation chromatography (GPC) was employed to determine the molecular weights and dispersities $Đ$, which are presented in Tables 1 and S1. The effect of the chain length on photocatalysis will be discussed later.

The polymers were initially characterized with regard to their properties in the solid state under dry conditions. The thermal stability was determined through a thermogravimetric analysis (TGA) conducted under nitrogen gas with a rate of 10 K min^{-1}. Both polymers show thermal stability up to 370°C; the conventional DSC did not indicate any phase transitions (Figure S6), and the flash DSC also showed no such transitions (Figure S7). The optical absorption and photoluminescence data for the polymers are presented in Figure 2a,b. The respective thin film absorption onsets are presented in Table 1 as optical band gaps, E_{opt}. The two polymers exhibit a comparable onset energy. The bathochromic shift in the onset between absorption spectroscopy in solution and absorption spectroscopy in thin films can be attributed to aggregation in solution (Figure S8) [38, 39]. The absorption maximum at 380 nm can be attributed to the π-π absorption of the polymers. The more intense absorption located at 650 to 800 nm, depending on the polymer, is typically regarded as the internal charge transfer (ICT) band of the

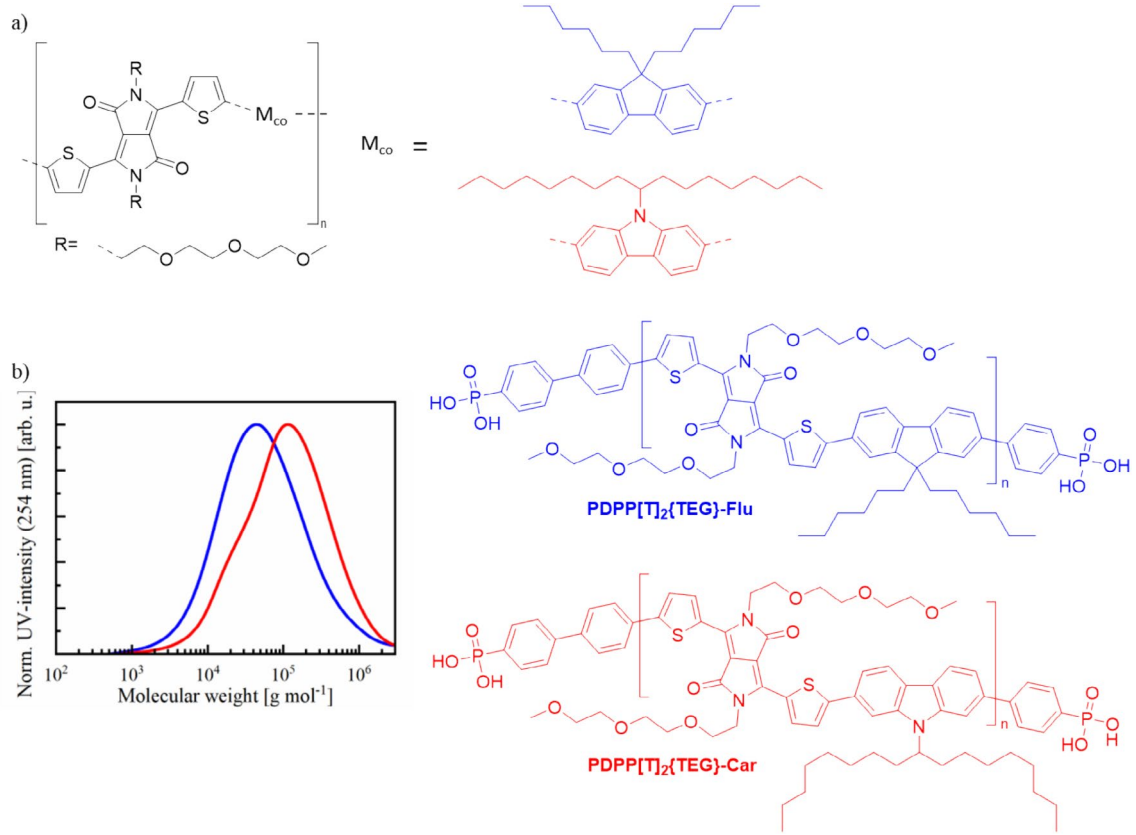

FIGURE 1 | (a) Representation of the synthesized polymers PDPP[T]$_2${TEG}-Flu and -Car. The synthesis was conducted thermally-assisted in an oil-bath well as in a microwave reactor. (b) Distribution of the molecular weight for PDPP[T]$_2${TEG}-Flu-3 and PDPP[T]$_2${TEG}-Car-3 with gel permeation chromatography in THF containing 0.25 wt.-% tetrabutylammonium bromide and PS calibration. Polymer structures of the respective synthesized polymers are given on the right.

TABLE 1 | Overview of the synthesized polymers and corresponding properties.

Polymer	Synthesis	M_n[a] (kg mol^{-1})	M_w (kg mol^{-1})	$Đ$[b]	$T_{5\%}$[c] (°C)	IP[d] (eV)	EA[e] (eV)	E_{CV}[f] (eV)	E_{opt}[g] (eV)
PDPP[T]$_2${TEG}-Flu-3	Oil bath	23.0	116.2	5.1	371	5.6	3.7	1.90	1.7
PDPP[T]$_2${TEG}-Car-3	Oil bath	42.5	187.2	4.1	378	5.1	3.7	1.90	1.7

[a]Determined by GPC using THF containing 0.25 wt% tetrabutylammonium bromide as the eluent.
[b]Dispersity.
[c]Temperature with 95% remaining mass taken from TGA measurements.
[d]Ionization potential (HOMO) measured by UPS.
[e]Electron affinity (LUMO) measured by E_{CV}.
[f]Band gap determined by cyclic voltammetry in a thin film.
[g]Optical band gap determined from absorption onset in film.

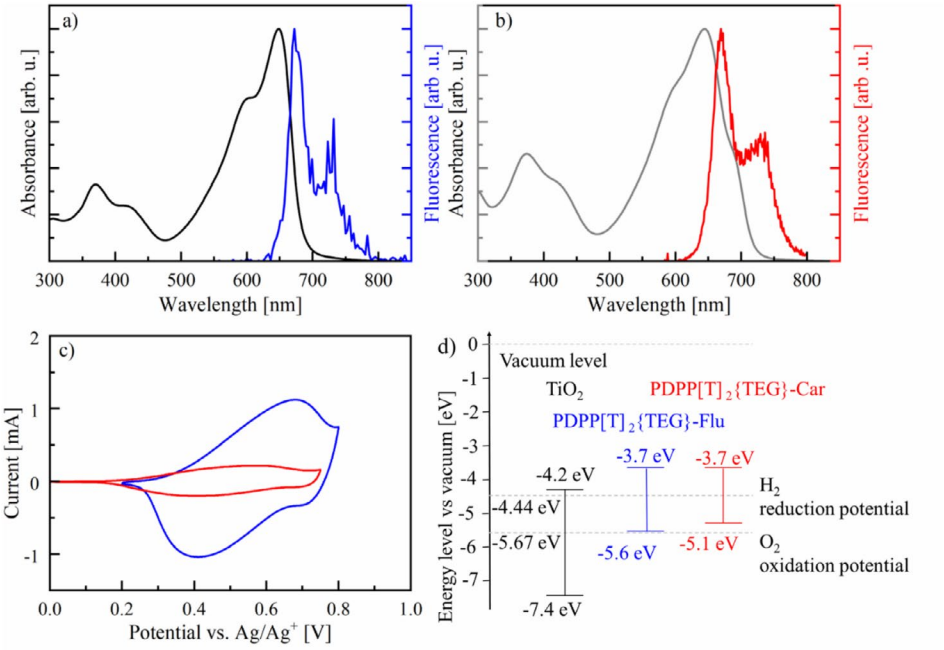

FIGURE 2 | UV–Vis and fluorescence spectra of (a) PDPP[T]$_2${TEG}-Flu-3 and (b) PDPP[T]$_2${TEG}-Car-2. Both spectra were each recorded in 0.1 mg ml^{-1} THF solution. (c) Cyclic voltammograms from thin film in acetonitrile at a scan rate of 100 mV s^{-1}. The data are plotted vs. Ag/Ag$^+$ and corrected to ferrocene. For both graphs, the blue graph shows the PDPP[T]$_2${TEG}-Flu-3 and the red one PDPP[T]$_2${TEG}-Car-3. (d) Band positions and band alignment in the aimed heterojunction.

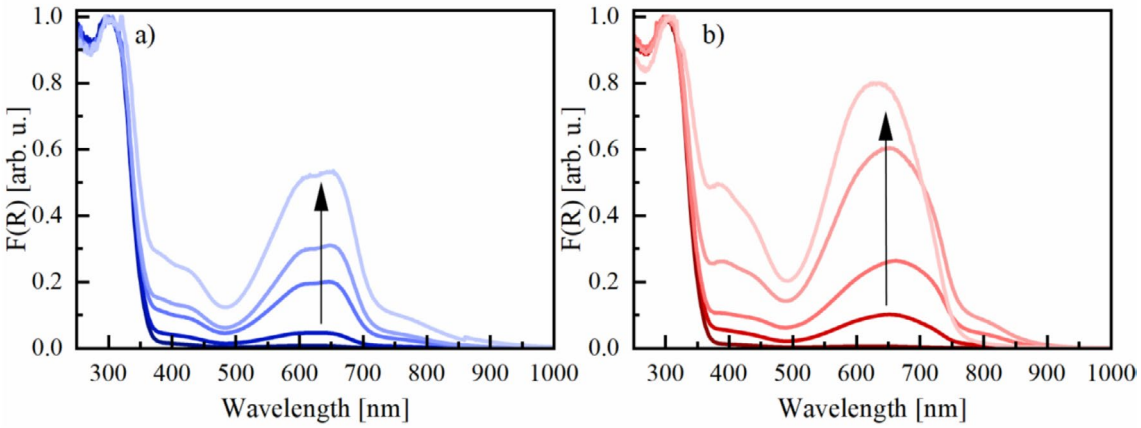

FIGURE 3 | UV–Vis characterization of the composite materials. (a) PDPP[T]$_2${TEG}-Flu-3 was used with an increasing amount of polymer. The absorption of the polymer increases with the used amount. (b) PDPP[T]$_2${TEG}-Car-3. All curves are normalized to the signal of TiO_2 at 300 nm.

ground state between donor and acceptor moieties of the polymer chain [40]. This bimodal absorption is characteristic of D-A polymers [19, 41, 42].

The photoluminescence spectra exhibit a similar bimodal distribution. The lifetime of the excited charges is 2.03 ns for PDPP[T]$_2${TEG}-Flu and 1.72 ns for PDPP[T]$_2${TEG}-Car, as illustrated in Figure S9 and Table S2. These values are comparable to those previously reported for DPPs in solution. In the case of PDPP[T]$_2${TEG}-Flu, the maximum at 671 nm, and in the case of PDPP[T]$_2${TEG}-Car, the maximum at 667 nm corresponds probably to the transition from 0 ➔ 0. The second peak at 728 nm and 731 nm is the 0 ➔ 1 transition [43]. This transition is observed as a second peak or shoulder, as the influence of the side chain on this transition is predominant. The two peaks are discernible due to the planar and rigid structure of the PDPPs, which reduces non-radiative decay pathways and results in distinguishable absorption and emission peaks [43, 44].

The two PDPP polymers were also characterized by FTIR spectroscopy. As illustrated in Figure S10, typical spectra display a dual band at 2980 and 2850 cm^{-1}, which can be attributed to the oscillation of the C—H bonds. The signal observed at 1660 cm^{-1} can be attributed to the tertiary amide bond present within the DPP core. The stretching vibration of the C═C bond of the DPP core serves to accentuate this signal. The bands observed at 1550 and 1450 cm^{-1} are indicative of the stretching vibration of the aromatic C═C. The broad band observed in the fingerprint region at 1090 cm^{-1} is attributed to the C—O vibration.

The band gap of the polymers was evaluated by cyclic voltammetry for the polymers PDPP[T]$_2${TEG}-Flu-3 and PDPP[T]$_2${TEG}-Car-3 as thin films on ITO substrates in acetonitrile (Figure 2c). The received cyclic voltammograms were corrected against ferrocene according to a published procedure [45]. The ionization potential (IP) values were also evaluated by UPS measurements (Figures S11 and S12).

It is important to distinguish between the optical gap, E_{opt}, and the electronic band gap obtained from cyclic voltammetry, E_{CV}. Similarly, IP values obtained from CV and UPS measurements will also differ due to stabilization effects based on the ambient conditions of the sample and the techniques employed in the measurement process. The optical gap (E_{opt}) is typically smaller than the band gap obtained from cyclic voltammetry. The discrepancy between the E_{CV} and E_{opt} can be conceptualized as the exciton binding energy, E_b ($E_b = E_{CV} — E_{opt}$). In the case of PDPPs, values between 0.09 and 0.5 eV have been reported [42, 46]. The exciton binding energy of 0.2 eV is in accordance with the anticipated value. The data regarding the band positions are presented in Figure 2d with the HOMO position calculated from UPS. The LUMO is calculated from the CV data. It is imperative that a heterojunction between TiO_2 and the polymers is formed to facilitate a successful charge transfer from the polymer to the inorganic semiconductor.

2.2 | Composite Materials

The resulting p-type polymers exhibit low-charge carrier mobility, which was confirmed by the evaluation of the charge carrier mobility conducted via bottom-gate bottom-contact organic field effect transistors (OFETs) devices (Figures S13 and S14; and Table S3). For better charge carrier separation, this necessitates interaction with, for example, a combined material [29, 33]. Thus, composite materials of TiO_2 (anatase, 20 nm, 100 $m^2 g^{-1}$) with the presented polymers were formed by dissolving the polymers in 10 mL tetrahydrofuran and the addition of 100 mg TiO_2. The amount of added polymer was varied from 0.1 wt.-% to 50 wt.-% (0.1 wt.-%, 1.2 wt.-%, 11.1 wt.-%, 33.3 wt.-%, 50 wt.-%). The received composites varied in color and loading.

The composites were further characterized in solid state. The x-ray diffractogram (XRD) reveals the presence of only the reflections characteristic of anatase (Figure S15). The successful formation of the composite was confirmed by diffuse reflectance infrared Fourier transformation spectroscopy (DRIFT) and solid-state ^{1}H MAS and ^{13}C MAS NMR spectra. The signals of the pristine polymer PDPP[T]$_2${TEG}-Flu-3 are discernible in the 11.1 wt.-% (1:8) composite (Figure S16). In the ^{1}H MAS NMR spectra, the signal at 5.96 ppm is attributed to the aromatic H signals present in the fluorene and thiophene comonomers. The signal at 3.23 ppm is attributed to the triethylene glycol side chain, while the aliphatic side chain is observed at 0.73 ppm. In the ^{13}C MAS NMR spectra, the signals for the polymer were discernible (Figure 6).

2.2.1 | Optical Properties and Loading

The composite materials were characterized by absorption spectroscopy in diffuse reflectance and visualized as Kubelka–Munk plots (Figure 3). They exhibit a maximum absorption at a wavelength of 630 nm. This is consistent with the observed maximum for the pristine polymers. The incorporation of TiO_2 introduces an additional absorption edge at 360 nm. As the quantity of polymer incorporated into the composite material is increased, the observed polymeric absorption increases. The absorption observed at 300 nm is attributed to the absorption of the TiO_2 material, and the absorption of the polymer is superimposed upon that of the inorganic material. The data confirm that the PDPPs and TiO_2 have been successfully combined. The absence of a shift in the absorption maximum indicates that the adsorption is stable and that there has been no change in the dihedral angles of the molecule, since a change in the dihedral angles would lead to a blue shift of the maximum [39]. The structured absorption, which exhibits two distinguishable peaks at the maximum, is diminished for PDPP[T]$_2${TEG}-Flu-3 and absent for PDPP[T]$_2${TEG}-Car-3. This indicates that the polymer might form aggregates.

In order to evaluate the quantity of organic material present on the surface of the composite, the materials were subjected to thermal characterization (thermogravimetry) in air. As the quantity of polymer incorporated into the composite is increased, the amount of organic material present on the surface of the TiO_2 particles also increases (Figure S17). The additional washing step with tetrahydrofuran (THF) serves to remove any unabsorbed excess polymer from the surface. Scanning electron microscopy reveals an even distribution of the polymer on the surface of TiO_2 before photocatalysis (cf. Figure 4a) and after photocatalysis (cf. Figure 4b), as can be seen in comparison to bare TiO_2 (Figure S18). The lattice plains were observed in the transmission electron microscopy (TEM) (c.f. Figure S19). The lattice structure is 0.35 nm and consistent with comparable reported values. The surface coverage of the polymer has a thickness of 1.2 nm [28, 47].

To guarantee the stability of the resulting composites, one sample was subjected to a thorough cleansing process with THF by Soxhlet extraction. The quantity of organic matter in the composite was found to be approximately equivalent to that observed in the control sample that had undergone the standard washing procedure. No discernible difference was observed in the optical properties or the DRIFT spectrum. The quantity of organic mass is diminished, yet within each sample with an identical weight ratio, there is invariably a degree of discrepancy (Figure S20).

2.3 | Photocatalysis

The composite materials with varying loadings were evaluated for their photocatalytic activity in hydrogen evolution under simulated sunlight. Figure 5a illustrates that the hydrogen evolution rate remains constant for all ratios, with the exception of the 1:8 ratio (11.1 wt.-%), which exhibits a slight decrease in the rate over time. Nevertheless, all composites demonstrated a sustained generation of hydrogen under solar irradiation with stable gas evolution rates.

All experiments were initiated at the same time and commenced at the same point in time. The addition of rare metals

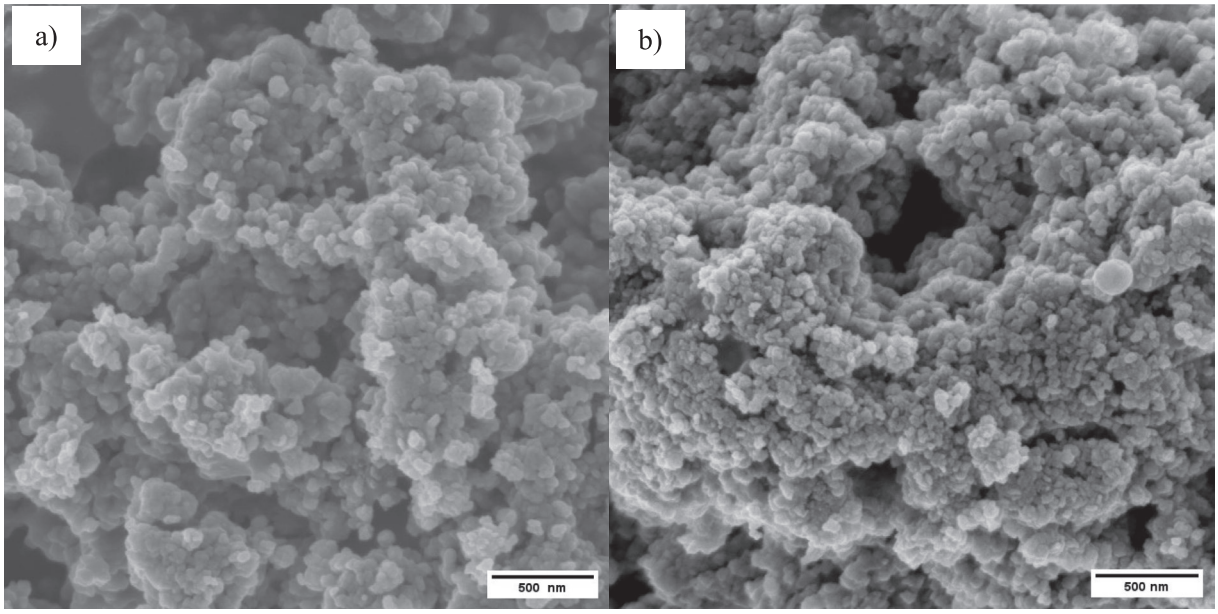

FIGURE 4 | Comparison of the composite material surface before (a) and after the photocatalysis (b). The images were taken with the InLens detector.

as co-catalysts, such as platinum, was not employed. X-ray photoelectron spectroscopy (XPS) characterization of the pristine polymer reveals the absence of Pd signals, which may have been attributed to the residual presence of palladium in trace amounts resulting from the Suzuki–Miyaura synthesis (Figure S21) that could act as co-catalysts. Thus, no residual metal acts as a catalyst here.

All composite materials exhibit enhanced activity relative to pristine TiO_2 (cf. Figure 5b); the incorporation of either polymer results in an elevated hydrogen evolution rate compared to pristine TiO_2. It was observed that an increase in the quantity of organic material present on the inorganic semiconductor did not necessarily result in higher rates of hydrogen evolution. The optimal ratio of polymer to inorganic semiconductor is 1:8 (11.1 wt.-% polymer), as this ratio exhibits the highest rate of hydrogen evolution and the highest accumulated amount of evolved hydrogen up to a rate of 8.06 μmol h^{-1} and 19.01 μmol of evolved hydrogen over 3 h, respectively.

Tests without sacrificial agent show no hydrogen evolution. To allow efficient charge separation and redox process in the composite, a hole scavenger must be added. This indicates the necessity of ethanol as a sacrificial agent. The highest hydrogen evolution rates were observed for the composite material comprising PDPP[T]$_2${TEG}-Flu. The maximum at a polymer ratio of 1:8 can be explained by the fact that, with an increase in the amount of polymer, the color of the composite darkens. This has the effect of inhibiting light penetration. Furthermore, the surface of the TiO_2 is increasingly covered in polymer, which results in the active sites being inaccessible for successful hydrogen evolution.

For PDPP[T]$_2${TEG}-Car, the three smallest amounts of polymer on the surface give similar results (see Figure 5d). Again, all composite materials exhibit a consistent hydrogen evolution rate over a three-hour period, indicating a sustained generation of hydrogen gas under illumination. In this instance, the hydrogen evolution rate is observed to be lower for the two highest ratios and is also smaller than that observed for 1:800 (0.1 wt.-%) and 1:8 (11.1 wt.-%). One potential explanation for this phenomenon is that the active sites of the inorganic semiconductor are too extensively covered by the polymeric mass, thereby preventing effective participation in photocatalysis at high loadings. The darkened color of the materials and the larger polymer amounts result in increases shadowing effects, which in turn leads again to a decrease in the light penetration. Nevertheless, only a minimal quantity of the polymer is necessary for the generation of charge carriers and their transfer from the polymer to TiO_2.

An examination of the cumulative amounts of H_2 (Figure 5f) reveals a distinct disparity between ratios of 1:8 and 1:2 (33.3 wt.-%), with composite materials exhibiting loading ratios of 1:800 to 1:8, demonstrating a uniform evolution of all three around 11.43 to 9.66 μmol. Ratios of 1:2 and 1:1 exhibit a mere 2.04 to 4.57 μmol. In the case of the 1:1 ratio, no increase is observed in comparison to the pristine TiO_2 sample.

In this instance, the observed trend differs from that observed with PDPP[T]$_2${TEG}-Flu. The composite materials demonstrate a greater quantity of H_2 for those comprising a higher proportion of polymer, with the influence of the polymer becoming evident at a ratio of 1:8. Regarding the carbazole copolymer, it can be observed that the polymer exerts an influence on the production of hydrogen gas at relatively low concentrations of polymer. The ratio of 1:8 was identified as the most effective for both composites, indicating that only a minimal quantity of the composite material is necessary to enhance H_2 evolution.

Also, there is an activity difference between the two polymers. The composite formed with PDPP[T]$_2${TEG}-Flu provides a higher activity than the composite of PDPP[T]$_2${TEG}-Car. One possible reason may be the difference in the charge carrier

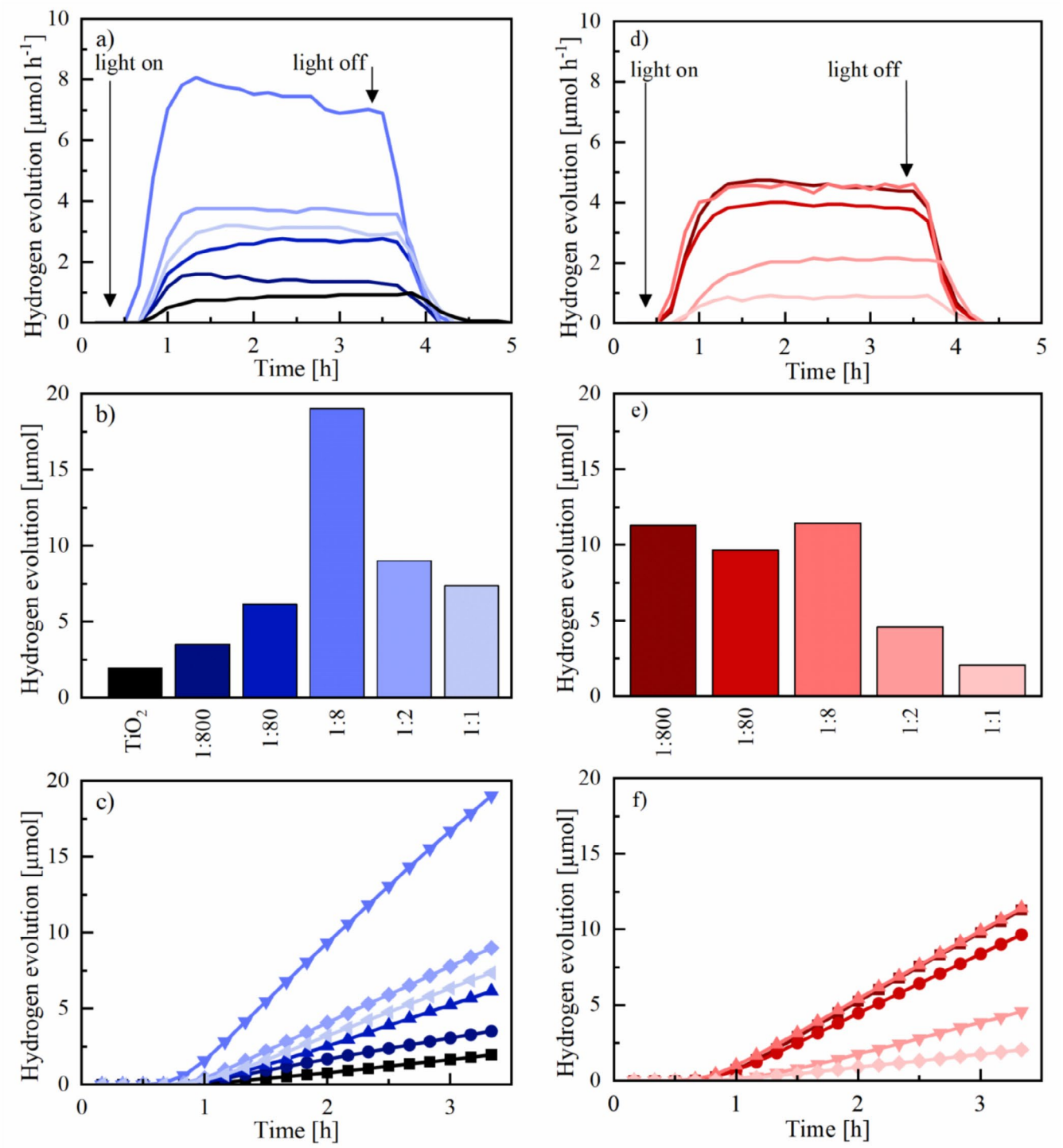

FIGURE 5 | (a-c) Results of the photocatalytic activity of the composite materials PDPP[T]$_2${TEG}-Flu-3 and TiO_2. The black curves are pristine TiO_2. Dark blue: 1:800 (0.1 wt.-%) to light blue: 1:1 (50 wt.-%) ratio. (a) Hydrogen evolution rate of the composite material of PDPP[T]$_2${TEG}-Flu-3 and TiO_2. (b) Cumulated evolved hydrogen other the illumination time of 3 h. (c) Accumulated hydrogen evolution plotted against the time. (d-f) Results of the photocatalytic activity of the composites of PDPP[T]$_2${TEG}-Car-3 and TiO_2. Dark red: 1:800 (0.1 wt.-%) to light red: 1:1 (50 wt.-%) ratio. (d) Hydrogen evolution rate of the composite material of PDPP[T]$_2${TEG}-Car-3 and TiO_2. (e) Cumulated evolved hydrogen over the illumination time of 3 h. (f) Accumulated hydrogen evolution plotted against the time.

lifetime observed in the fluorescence measurement. For the carbazole copolymer, the charge carrier lifetime is shorter (1.72 ns) than for the fluorene copolymer with 2.03 ns (c.f. Table S2). Hence, the losses to recombination may be bigger for PDPP[T]$_2${TEG}-Car-composite materials. Another reason for the activity difference can be the difference in the surface bonding between the fluorene comonomer and the carbazole comonomer. As found for PDPP-Car, photocatalytic activity for dye degradation increases with better contact between polymer and TiO_2 [28]. The carbazole side chain is longer as well as more

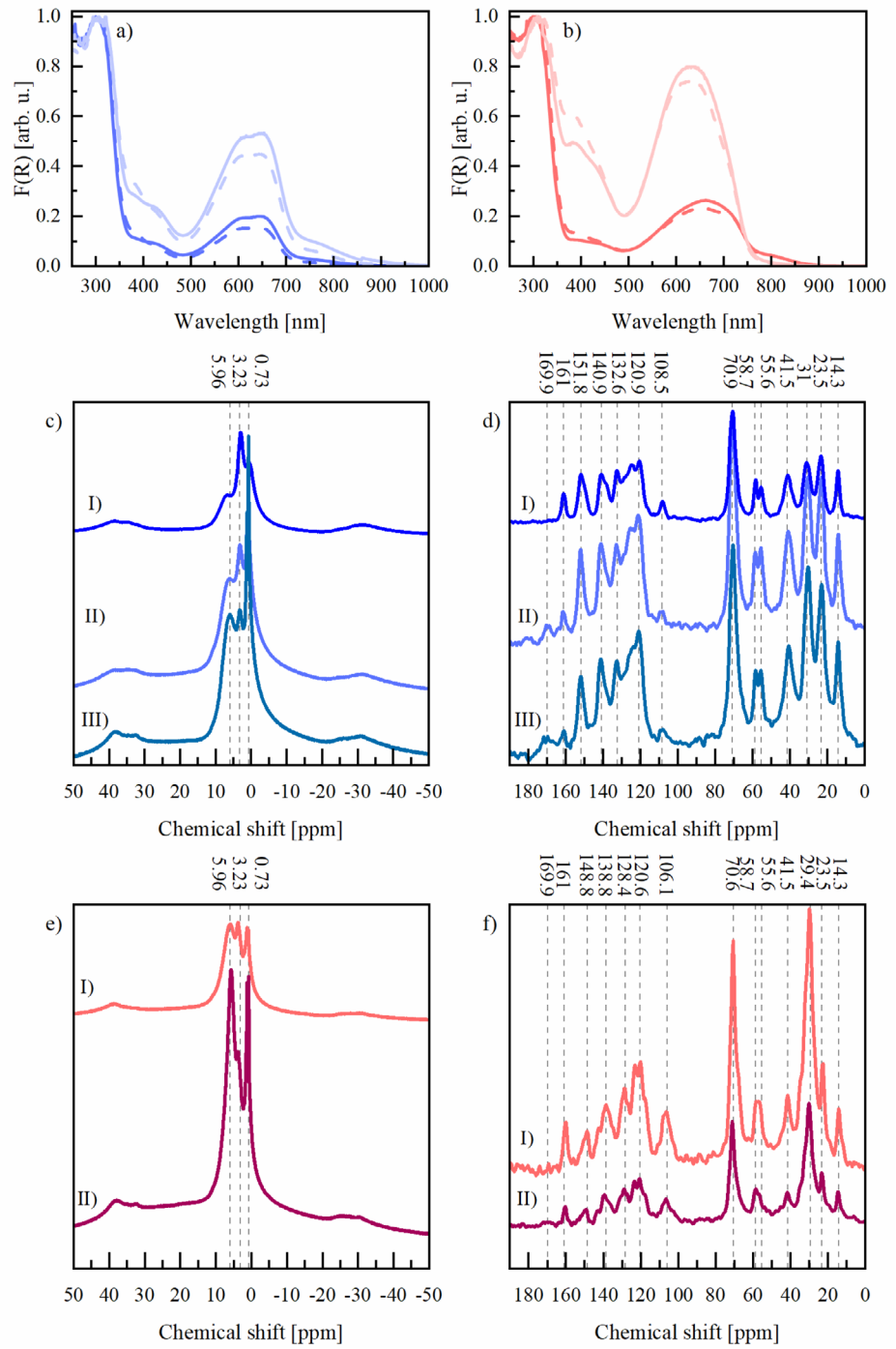

FIGURE 6 | Comparison of the intensity decrease of the composite materials. (a) In blue: PDPP[T]$_2${TEG}-Flu on TiO_2 in blue the 1:8 ratio and in light blue 1:1. The compact line is the signal before photocatalysis and the dotted line after photocatalysis. (b) The same comparison for PDPP[T]$_2${TEG}-Car. All curves are normalized to the signal of TiO_2 at 300 nm. (c) ^{1}H MAS solid-state NMR spectra of PDPP[T]$_2${TEG}-Flu. (d) ^{13}C MAS solid state NMR spectra. (I) The pristine polymer PDPP[T]$_2${TEG}-Flu, (II) The composite with a ratio of 1:8 before photocatalysis. (III) After photocatalysis. (e) ^{1}H MAS solid-state NMR spectra. (f) ^{13}C MAS solid state NMR spectra of PDPP[T]$_2${TEG}-Car, (I) The composite with a ratio of 1:8 before photocatalysis. (II) After photocatalysis.

moveable, as the N moiety provides better flexibility at position 9 due to the sp^2 hybridization of the N.

As the fluorene derivative is more rigid, the interaction with the TiO_2 may be more favorable, as the packing order is stabilized by the rigidity. Experiments, such as GIWAXS characterization, are necessary to elucidate this further. In general, carbazole is a different donor molecule than fluorene and provides a different activity, as the D-A structure is different.

The catalytic activity is derived from the interaction between the polymers and the inorganic semiconductor. TiO_2 alone demonstrated a lower hydrogen evolution rate. In the same manner, PDPP[T]$_2${TEG}-Flu exhibits no activity toward hydrogen

evolution in 10 vol.-% ethanol without TiO_2. Furthermore, upon the use of ascorbic acid (6.6 g in 150 mL, 0.25 mol L^{-1}, neutralized with 6 mL 1 M NaOH) as a sacrificial agent and illumination for 3 h under closed-loop circulation, no hydrogen evolution is observed for neat PDPP[T]$_2${TEG}-Flu.

The polymer demonstrated stability under repeated light exposure, as evidenced by the GPC characterization and ^{1}H-NMR, which showed no degradation (Figures S22 and S23). The UV region beneath 420 nm is crucial for hydrogen evolution. Tests conducted with illumination at wavelengths exceeding 420 nm demonstrated the absence of activity toward hydrogen evolution. The activity of TiO_2 in the UV region is necessary for hydrogen evolution. The expansion to the visible light by the usage of the conjugated polymers increases the amount of exploited sunlight. Nevertheless, the excitation of TiO_2 remains crucial.

The deposition of co-catalysts via photolysis can serve to reduce the activation energy and overpotential for the HER [48]. Thus, TiO_2 was decorated with 0.2 wt.-% platinum by photodeposition. The formation of composite materials with these inorganic semiconductors has been observed to result in a higher hydrogen evolution rate than that observed in the absence of platinum. None of the composites exhibited a hydrogen evolution rate that surpassed that of the pristine TiO_2 with 0.2 wt.-% Pt. The hydrogen evolution of composite materials was enhanced by the photodeposition of 0.2 wt.% Pt, yet it did not reach the level observed for the pristine TiO_2 with Pt. These findings suggest that the active site for the HER is the TiO_2 semiconductor. The addition of Pt increases the hydrogen evolution rate, but the activity is slightly decreased when the surface is covered with organic mass, in comparison to pristine TiO_2 with 0.2 wt.-% Pt (see Figure S24).

In addition, one sample of a ratio of 1:8 (11.1 wt.-% PDPP[T]$_2${TEG}-Flu) was tested for an illumination time of 8 h. The hydrogen evolution was found to be constant over the observed time frame, indicating the stability of the composite material and the polymer. Post-catalytic characterization confirms the stability of the bandgap and structural stability of the polymer (see Figure S25; Table S4).

Post-catalytic characterization of the amount of organic mass on the inorganic substrate shows an increase in loading. The added sacrificial agent, ethanol, leaves residues on the surface (c.f. Figure S26).

The post-catalytic characterization, employing absorption spectroscopy, DRIFT, and solid-state NMR, revealed a reduction in the absorption of the internal charge transfer band normalized to the absorption of TiO_2. The optical band gap remained unaltered (Figure 6a,b, for more details, please refer to Table S4, Figures S27–29). The observed decrease in absorption can be attributed to the loss of contact between some of the polymer and the TiO_2 due to the rigorous stirring process, as investigated by ^{1}H MAS NMR spectroscopy shown in Figure 6c. An additional potential cause is the degradation of the polymer due to illumination. Nevertheless, degradation would result in a change to the optical band gap. Furthermore, the post-catalytic characterization of the polymer-only photocatalysis tests, which demonstrated no activity, revealed no change in the molecular weight distribution and ^{1}H-NMR (cf. Figures S22 and S23). It is, therefore, reasonable to deduce that some of the polymers not in direct contact with the TiO_2 may be lost over time through prolonged stirring. This will be addressed in future work.

The solid-state NMR analysis indicates a reduction in the intensity of the ^{1}H MAS signal at 3.20 ppm, which is attributed to the triethylene glycol (TEG) side chain (Figure 6c,e). For both polymers, the signal of the hydrophilic side chain is observed to decrease. It is possible that the TEG side chain is undergoing degradation, however, the signals for adsorbed H_2O are also present in the same region and overlap with this signal. Given that the signal intensity ratio shifts with the formation of composite materials, it can be posited that surface-adsorbed THF from the composite preparation may be influencing the intensity ratio from 3.20 to 0.73 ppm. Additionally, the observed increase in the signal at 0.73 ppm may be attributed to the adsorption of oxidized ethanol or THF on the TiO_2 surface. In the ^{13}C MAS spectra, the signal of the TEG chain is observed at 70.9 ppm for the chain and at 58.7 and 55.6 ppm for the end groups (Figure 6d,f). The stability of the TEG chain is indicated by the absence of any change in both signals. The signals of THF can be incorporated into the signals of the TEG side chain and the alkyl side chain, which are observed at 70.9 and 23.5 ppm, respectively. In general, the observed decrease in intensity for the C═O signal at 161.0 ppm may be attributed to the inherent limitations of the measurement setup, which is less optimally suited for the analysis of composite materials than for pristine polymers. The formation of the composite material results in the emergence of a second signal at 171.0 ppm, situated within the C═O region.

2.4 | Polymer Chain Length Variation

Furthermore, the influence of chain length on the photocatalytic hydrogen evolution of the PDPP copolymers in the PDPP-TiO_2 composites was investigated. Figure 7a,b shows the GPC curves for PDPP copolymers with fluorene as well as carbazole as the co-monomer from different syntheses. As the Suzuki polymerization process is dependent on the precise quantity of monomer at the outset, the resulting molecular weight is contingent upon the amount of monomer that is added. The resulting molecular weight distributions are presented in Table 2 for reference.

For the formation of composite materials, the best-performing ratio of 1:8 was used. In this case, the majority of composites exhibit enhanced activity compared to that of pristine TiO_2. As the chain length increases, the activity toward H_2 evolution also increases. The fluorene copolymer displays a higher level of activity than the carbazole copolymer. For PDPP[T]$_2${TEG}-Car-1, the amount of evolved hydrogen was found to be lower compared to pristine TiO_2 (Figure 7c). This indicates that the positive effect of adding a second semiconducting absorber is surpassed by the negative effect of active site inhibition. The photocatalytic activity of the PDPP[T]$_2${TEG}-Flu composites was observed to increase from 4.37 µmol after 3 h of illumination (PDPP[T]$_2${TEG}-Flu-1) to a maximum of 19.01 µmol for the best-performing material (PDPP[T]$_2${TEG}-Flu-3). A similar trend was observed for the PDPP[T]$_2${TEG}-Car, with a notable

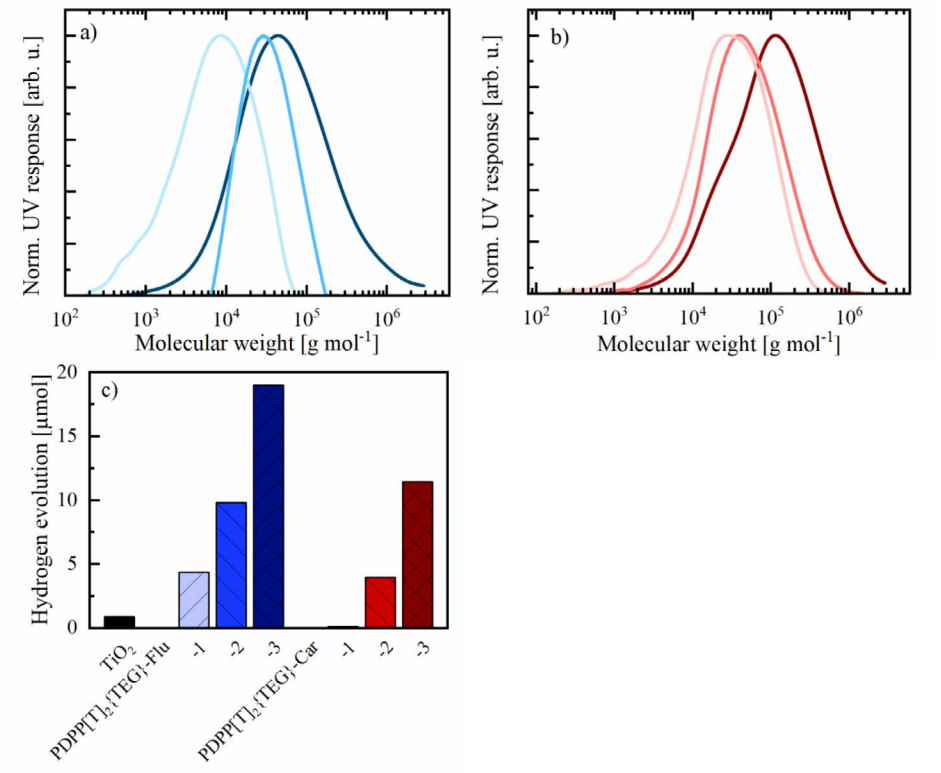

FIGURE 7 | GPC characterization of both polymers in THF containing 0.25 wt.-% tetrabutylammonium bromide and PS calibration. (a) PDPP[T]$_2${TEG}-Flu shows for synthesis 1 (light blue) a smaller molecular weight than synthesis 2 (blue) and synthesis 3 (dark blue). (b) PDPP[T]$_2${TEG}-Car the molecular weight distribution increases similarly to the fluorene copolymer. Batch 1 (light red) has the smallest molecular weight, and the molecular weight increases with different syntheses. (c) Comparison of the accumulated hydrogen after 3h for different composites with varying chain lengths. The chain length increases from 1 to 3 and corresponds to the names in Table 2.

TABLE 2 | Comparison of the molecular weight distribution of the different polymer syntheses.

Polymer	Synthesis	Endcapper	M_n [a] (kg mol^{-1})	M_w (kg mol^{-1})	$Đ$
PDPP[T]$_2${TEG}-Flu-1	Oil bath	Brombenzene	3.5	11.9	3.3
PDPP[T]$_2${TEG}-Flu-2	Microwave	Brombenzene	25.5	39.7	1.6
PDPP[T]$_2${TEG}-Flu-3	Oil bath	Phosphonic acid	23.0	116.2	5.1
PDPP[T]$_2${TEG}-Car-1	Oil bath	Phosphonic acid	11.5	47.7	4.4
PDPP[T]$_2${TEG}-Car-2	Oil bath	Phosphonic acid	24.2	75.0	3.1
PDPP[T]$_2${TEG}-Car-3	Oil bath	Phosphonic acid	42.5	187.2	4.1

increase in activity from 0.10 µmol (PDPP[T]$_2${TEG}-Car-1) to 11.43 µmol (PDPP[T]$_2${TEG}-Car-3). Therefore, it can be concluded that an increased chain length is beneficial for photocatalytic activity. All polymers remained soluble in tetrahydrofuran and chloroform. This opens the opportunity to utilize the polymers out of solution, for example, as thin film or additional layer in photoelectrodes in the future.

As previously stated, the excitation of the inorganic semiconductor TiO_2 is crucial for the hydrogen-evolving activity. The polymer acts as a sensitizing agent with favorable band alignment to enhance the activity. Both the polymer and TiO_2 are generating charge carriers upon illumination, and the active site as a catalyst is the TiO_2.

The combination of PDPP and TiO_2 has been observed to enhance the rate of hydrogen evolution as compared to that in Table 3. It is also possible to achieve the same effect by adding rare metals such as Pt as cocatalysts. Nevertheless, it has been demonstrated that the incorporation of organic semiconductor polymers can yield comparable outcomes, with an eightfold enhancement in the hydrogen evolution rate observed with these earth-abundant polymers. This trend is analogous to the findings of Yang et al. regarding methyl orange degradation. They also observed a dependence on the molecular weight of the PDPP chain length [28]. However, the present study demonstrates for the first time a correlation between the hydrogen evolution rate and the PDPP chain length in PDPP-TiO_2 composites.

TABLE 3 | Comparison of the best-performing hydrogen evolution of our composite with literature composite materials with TiO_2.

Polymer	Amount of polymer	Amount of photocatalyst	Added cocatalysts	Hydrogen evolution	Sacrificial agent	Ref.
B-BT-1,4-E	16.7%	30 mg	None	220.4 μmol h^{-1}	TEOA	[24]
n-IEP-20@T-10	10 wt.-%	25 mg	Residual Pd	81 μmol h^{-1}	Methanol	[25]
TiO_{2-X}-P3 (PB2T-TEG)	3 wt.-%	1 mg	0.62 wt%	35.7 μmol h^{-1}	TEOA	[26]
DPP dye	0.05 μmol	2.5 mg	Pt	8.4 μmol h^{-1}	AA	[27]
PDPP-Car	2 wt%	100 mg	Residual Pd	MO degradation	—	[28]
BFBA	4%	30 mg	Residual Pd	220.2 μmol h^{-1}	TEOA	[49]
Poly(benzothiadiazole) BBT	6.7 wt.-%	30 mg	0.5 wt% Pt	178 μmol h^{-1}	TEOA	[50]
PDPP[T]$_2${TEG}-Flu-3	11.1 wt.-%	60 mg	None	8.06 μmol h^{-1}	Ethanol	This work

3 | Conclusion

This study investigated the hydrogen evolution of composite materials of PDPP and TiO_2. Two different polymers were synthesized and characterized thoroughly. The DPP core is modified with a hydrophilic side chain to increase its solubility. Fluorene and carbazole are polymerized with the DPP core as donor monomers. The UPS results show a suitable band alignment in terms of photocatalytic hydrogen evolution in combination with TiO_2. The addition of different ratios of polymer to TiO_2 results in various composite materials. UV–Vis results indicate the addition of the absorption of the polymer to the TiO_2 and a shift toward the visible light, thus a wider part of the solar spectrum is utilized. Photocatalytic hydrogen evolution activity tests show an increase in activity up to a polymer-TiO_2 ratio of 1:8 (11.1 wt.-% polymer). Higher amounts of polymer do not show any further increase. Nevertheless, a dependence of the hydrogen evolution activity on the chain length of the added polymer is found. A longer polymer chain results in increased hydrogen evolution rates. These results provide detailed insights into the formation of composite materials between PDPP polymers and TiO_2 and the need to characterize the chain length carefully as it influences the activity of such composites strongly.

4 | Experimental Section/Methods

4.1 | Materials and Methods

All reagents were used without further purification unless otherwise noted.

1,4-Benzenediboronic acid bis (pinacol) (97%), Aliquat 336, Diethyl succinate (> 99%), N-Bromsuccinimid (99%), Potassium phosphate tribasic (98%), triphenylphosphine (for synthesis), Tris(dibenzylideneacetone)dipalladium (0) (97%), triethylene glycol monomethyl ester (95%) were purchased from Sigma Aldrich chemistry. 2,7-Bis(4,4,5,5-tetramethyl-1,3,2-dioxaborolan-2-yl)-9,9-dihexylfluorene (98%), 2-Cyanothiophene (98%), (4-Bromophenyl)phosphonic (98%) 9-(9-Heptadecanyl)-2,7-bis(4,4,5,5-tetramethyl-1,3,2-dioxaborolan-2-yl)carbazole (97%), Sodium tert-pentoxid (> 97%) were bought from TCI. Hombikat N100 anatase was received from Sachtleben. Ethanol, hexane, acetone, tetrahydrofuran, toluene (extra dry 99.85%), and chloroform were received from VWR and Fisher Scientific.

Microwave reactions were conducted in sealed vials using an Anton Paar Monowave 400. The polymer syntheses and characterization are described in detail in the Supporting Information. For the composite materials, 100 mg of TiO_2 (anatase, < 100 nm) were stirred overnight together with the corresponding amount of polymer in 10 mL tetrahydrofuran (THF) (analytical grade). After mixing the solution of PDPP[T]$_2${TEG}-Flu and TiO_2, the solid contents were separated by centrifugation. The powders were washed with THF and ultrapure water and dried in a drying oven at 80°C.

^{1}H-NMR spectra (300 MHz) were performed using a Bruker AC 300 spectrometer and calibrated according to the solvent resonance signal.

GPC measurements were measured using a Waters 515 HPLC pump and a column setup comprising a guard column (Agilent PLgel Guard MIXED-C, 5 × 0.75 cm^2, particle size 5 μm) and two separation columns (Agilent PLgel MIXED-C, 30 × 0.75 cm^2, particle size 5 μm). THF with 0.25 wt% tetrabutylammonium fluoride (TBAF) was used as an eluent. Polymer size distributions were monitored with a Waters 998 photodiode array detector. Narrowly distributed polystyrene standards were used for calibration and 1,2-dichlorobenzene as an internal reference. The samples were prepared by the addition of THF to 0.5–1 mg of the polymer and the solvation of the aforementioned. The syringe-filtered solution was transferred into a GPC vial. Molecular weights were given according to the PS calibration.

DRIFT spectra were measured on a Bruker Alpha II with the software OPUS. The resolution was set to 4 cm^{-1} with a sample scan time of 40 scans. Data were measured from 4000 to 350 cm^{-1}.

Cyclic voltammetry measurements were conducted using a Gamry Interface 1010 Potentiostat/Galvanostat, using a three-electrode setup and measured in acetonitrile with tetrabutylammonium hexafluorophosphate ($TBAPF_6$) (0.1 M) as electrolyte for the band gap determination. The substrates

were polymer thin-films spin-coated (1000 min^{-1}, 60 s, 40 µL) on ITO substrates from THF (5 mg mL^{-1}). As a counter electrode, a Pt electrode was used in combination with a standard $Ag/AgNO_3$ reference electrode in acetonitrile. The electrolytes were degassed with nitrogen for 5 min before the measurements. The scans were recorded at a scan rate of 50 or 100 mV s^{-1}, with a step size of 2 mV. The values were corrected versus the ferrocene (Fc/Fc^+) redox couple as a reference. The IP and EA values were calculated considering the solvent effects as published [41].

UV–Vis–NIR measurements on thin films were performed by a Jasco V-670 spectrometer. Thin films were prepared by spin-coating from THF (5 mg mL^{-1}) on cleaned Menzel glass slides (1000 min^{-1}, 60 s, 40 µL). The glass was cleaned with ultrasonication in Hellmanex (2 wt%), water, acetone, and isopropanol for 15 min each and dried with a nitrogen jet. Before spin-coating, the slides were treated in an ozone oven (FHR). The measurements were recorded with a Menzel slide as a reference between 300 nm and 2000 nm. The Menzel slides were irradiated for 1 to 2.5 h under an Oriel sun simulator (AM 1.5, 1000 W m- 2) for light stability tests and measured again.

Solid-state and solution absorption measurements were performed with a Perkin Elmer Lambda 750 device. Solid powder samples were characterized between 2000 to 200 nm. The step width was 1 nm. For solid samples, a Praying Mantis (Harrick) was employed. As a white standard, Spectralon was used. The polymers in the solution were measured at a concentration of 0.01 mg/mL.

XRD measurements on powder samples were performed on a PANalytical Empyrean with a Bragg–Brentano geometry. The device was equipped with a Cu tube for Kα irradiation (1.5406 Å) and a fixed anti-scatter slit of 1°. The powder was measured on a spinning sample holder with a PixCel detector between 10.016° and 80.000°. The step size was 0.066°.

Scanning electron microscope images were recorded on a Zeiss Leo 1530 with an acceleration voltage of 3 kV. The aperture size was 30.0 µm. As a detector, an InLens or an SE2 detector was used. The samples were sputtered with platinum to prevent charge accumulation (Cressington Sputter Coater 208HR).

For TEM measurements, a 200 kV JEOL-JEM-2100 was used. The setup is equipped with a Schottky FEG and an omega in-column energy filter. For lattice structure and interface thickness evaluation, ImageJ was used.

DSC measurements were performed with a Mettler Toledo TGA/DSC 3+ instrument operating under air atmosphere from 25°C to 750°C with a heating rate of 10 K min^{-1}. To eliminate water content, the sample was heated up to 120°C for 15 min. After cooldown to 25°C, the probe was heated up to 750°C with a heating rate of 10 K min^{-1}.

XPS measurements were performed with a PHI 5000 VersaProbe III system with an Al K_α source (1486.6 eV) and a dual neutralizer (electron gun and Ar^+) at 10 mbar. The survey and high-resolution spectra were observed from a 5 × 5 cm^2 area, selected by secondary electron imaging technique (SXI), and an x-ray source diameter of 100 mm. The evaluation was executed with a Multipak software from the manufacturer.

Samples were measured with a spectrometer Bruker Avance III 40 0 (Magnetic Field 9.4 T). They were spun at 12.5 kHz in a 3.2 mm MAS triple resonance probe (also Bruker).

The ^{13}C NMR MAS spectra were obtained using a ramped cross-polarization (CP) experiment, where the nutation frequency on the proton channel was varied linearly by 50%. The corresponding nutation frequency on the 13C channel and the contact time were adjusted to 60 kHz and 1 ms, respectively. During acquisition, proton broadband decoupling was applied using a spinal-64 sequence with a nutation frequency of 60 kHz. The ^{13}C spectra are referenced indirectly with respect to tetramethylsilane (TMS) using adamantane as a secondary reference.

For ^1H NMR we used a one pulse—experiment, where the 90° pulse length was set to 2.6 µs and the recycle delays were chosen long enough to have quantitative results (4 s).

The ^1H spectra are referenced using adamantane as a secondary reference ($\sigma(iso) = 1.8$ ppm) with respect to tetramethylsilane (TMS) ($\sigma(iso) = 0.0$ ppm).

Organic field-effect transistor devices with a bottom-gate bottom-contact geometry were obtained from Fraunhofer IPMS. The transistors consist of n-doped silicon oxide wafers with patterned interdigitated gold electrodes with a width of 10 nm and a length of 2.5, 5, 10, or 20 µm. The channel material was spin-coated (1000 min^{-1}, 60 s, 40 µL) from a 1 wt.-% solution in THF. The substrates were treated by ultrasonication in acetone and isopropanol to remove the photoresist layer and afterward for 15 min at 50°C in the ozone oven. The devices were treated for 2 h with HMDS at 140°C. The substrates were washed with isopropanol and dried with a nitrogen jet. The channel material was spin-coated (1000 min^{-1}, 60 s, 40 µL) from a 1 wt.-% solution in THF. I-V characteristics were measured using an Agilent Technologies B1500A Semiconductor Device Analyzer. The samples were annealed at 180°C for 10 min. The charge carrier mobility was extracted from the slope of the transfer characteristics ($I_{d0.5}$ vs. V_g) using Equation (1)

$$I_d \approx \frac{W}{2L} C_i \mu \left(V_g - V_T\right)^2 \quad (1)$$

with I_d as the drain current, W as the channel width, L as the channel length, C_i as the capacitance, V_g as the gate voltage, and V_t as the threshold voltage.

Time-dependent fluorescence measurements were conducted on a PicoQuant FluoTime 300 spectrometer with a VisUV-Laser (532 nm) and a 300 W Xenon lamp. The measurements were made in a 0.01 mg mL^{-1} polymer solution of THF and $CHCl_3$.

UPS measurements were carried out on a PHI 5000 VersaProbe III system. A He discharge light source provided stable and continuous He I and He II lines. The measurement was conducted

under ultrahigh vacuum (10^{-7} mbar). Polymer samples were prepared by spin-coating from THF (5 mg mL^{-1}) on clean ITO substrates. They were cleaned with ultrasonication in Hellmanex (2 wt%), water, acetone, and isopropanol for 15 min each and dried with a nitrogen jet. Before spin-coating, they were treated for 15 min in an ozone oven (FHR).

The photocatalytic hydrogen evolution reaction was performed under simulated solar light irradiation under continuous argon flow. 60 mg of the powder sample was dispersed ultrasonically in about 20 mL of water for 10 min. The dispersion was transferred into a glass reactor and water was added until 135 mL was reached. 15 mL of ethanol (analytical grade, VWR chemicals) was added and a total concentration of 10 vol% ethanol in water was achieved. To remove air, argon was bubbled through the reactor for 40 min at 100 mL min^{-1} or overnight at 25 mL min^{-1} (Bronkhorst mass flow controller). The reactor temperature was kept at 20°C (10°C for overnight bubbling) by a LAUDA cryostat. For the hydrogen evolution reaction, the gas stream was set to 25 mL min^{-1} and the stirred reactor was irradiated for 3 h with a 300 W Xe lamp (LOT QuantumDesign) with an AM 1.5G filter. The H_2 evolution was detected with a gas chromatograph (Shimadzu GC-2014). Wavelength-dependent measurements were conducted by adding a filter for wavelengths cutting off the wavelengths beneath 420 nm on top of the glass reactor (Schott-GG420). After the photocatalytic experiment, the samples were collected by centrifugation, separated by centrifugation from the reaction solution, and dried at 80°C.

Acknowledgments

The authors thank the Bavarian Polymer Institute (BPI), University of Bayreuth, for the use of XPS, UPS, TEM and SEM in the KeyLabs "Device Engineering" and "Electron and Optical Microscopy", and the Chair of Macromolecular Chemistry 1 for the use of the TGA and flash-DSC. The authors further thank Sebastian Städter and Robert Bätz for GPC measurements, Beate Bojer for solid state-NMR, Kerstin Hannemann for ^{1}H and ^{13}C-NMR, Lion Schumacher for XPS measurements, Dr. Jana Timm for help with the PL measurements, Jonas Jungmann for TEM measurements, Andreas Erhardt and Gert Krauss for partially monomer synthesis, Dennis Schröder for ^{31}P-NMR measurements, Florian Meichsner for help with the OFET measurement, and Felix Wenzel for help with the flashDSC measurement (all University of Bayreuth). The authors gratefully acknowledge funding by the Bavarian State Ministry of Science, Research and the Arts within the collaborative research network Solar Technologies Go Hybrid. T.M. thanks the Elite Study Program Macromolecular Science within the Elite Network of Bavaria (ENB) for support and the Graduate School of the University of Bayreuth.

References

1. K. Calvin, D. Dasgupta, G. Krinner, et al., *Climate Change 2023: Synthesis Report. Contribution of Working Groups I, II and III to the Sixth Assessment Report of the Intergovernmental Panel on Climate Change*, ed. H. Lee and J. Romero (IPCC, 2023).

2. S. Chu and A. Majumdar, "Opportunities and Challenges for a Sustainable Energy Future," *Nature* 488 (2012): 294–303.

3. A. Fujishima and K. Honda, "Electrochemical Photolysis of Water at a Semiconductor Electrode," *Nature* 238 (1972): 37–38.

4. B. Moss, Q. Wang, K. T. Butler, et al., "Linking In Situ Charge Accumulation to Electronic Structure in Doped SrTiO(3) Reveals Design Principles for Hydrogen-Evolving Photocatalysts," *Nature Materials* 20 (2021): 511–517.

5. Y. Ham, T. Hisatomi, Y. Goto, et al., "Flux-Mediated Doping of Srtio-3photocatalysts for Efficient Overall Water Splitting," *Journal of Materials Chemistry A* 4 (2016): 3027–3033.

6. T. Takata, J. Jiang, Y. Sakata, et al., "Photocatalytic Water Splitting With a Quantum Efficiency of Almost Unity," *Nature* 581 (2020): 411–414.

7. Y. Goto, T. Hisatomi, Q. Wang, et al., "A Particulate Photocatalyst Water-Splitting Panel for Large-Scale Solar Hydrogen Generation," *Joule* 2, no. 3 (2018): 509–520, https://doi.org/10.1016/j.joule.2017.12.009.

8. X. Yang, A. Wolcott, G. Wang, et al., "Nitrogen-Doped ZnO Nanowire Arrays for Photoelectrochemical Water Splitting," *Nano Letters* 9 (2009): 2331–2336.

9. A. Wolcott, W. A. Smith, T. R. Kuykendall, Y. Zhao, and J. Z. Zhang, "Photoelectrochemical Study of Nanostructured ZnO Thin Films for Hydrogen Generation From Water Splitting," *Advanced Functional Materials* 19 (2009): 1849–1856.

10. Y. Wang, A. Vogel, M. Sachs, et al., "Current Understanding and Challenges of Solar-Driven Hydrogen Generation Using Polymeric Photocatalysts," *Nature Energy* 4 (2019): 746–760.

11. C. M. Aitchison, M. Sachs, M. A. Little, et al., "Structure–Activity Relationships in Well-Defined Conjugated Oligomer Photocatalysts for Hydrogen production From Water," *Chemical Science* 11 (2020): 8744–8756.

12. X. Chen, K. Geng, R. Liu, et al., "Covalent Organic Frameworks: Chemical Approaches to Designer Structures and Built-In Functions," *Angewandte Chemie International Edition* 59 (2020): 5050–5091.

13. J. Kosco, F. Moruzzi, B. Willner, et al., "Photocatalysts Based on Organic Semiconductors With Tunable Energy Levels for Solar Fuel Applications," *Advanced Energy Materials* 10 (2020) 2001935, https://doi.org/10.1002/aenm.202001935.

14. R. S. Sprick, J. X. Jiang, B. Bonillo, et al., "Tunable organic photocatalysts for visible-light-driven hydrogen evolution," *Journal of the American Chemical Society* 137 (2015): 3265–3270.

15. M. Sachs, R. S. Sprick, D. Pearce, et al., "Understanding Structure-Activity Relationships in Linear Polymer Photocatalysts for Hydrogen Evolution," *Nature Communications* 91 (2018): 1–11.

16. M. Goel, C. D. Heinrich, G. Krauss, and M. Thelakkat, "Principles of Structural Design of Conjugated Polymers Showing Excellent Charge Transport toward Thermoelectrics and Bioelectronics Applications," *Macromolecular Rapid Communications* 40, no. 10 (2019): 1800915, https://doi.org/10.1002/marc.201800915.

17. J. A. Schneider and D. F. Perepichka, "1. Design Principles for Organic Semiconductors," in *Advanced Materials* (De Gruyter, 2019), https://doi.org/10.1515/9783110537734.

18. Y. J. Cheng, S. H. Yang, and C. S. Hsu, "Synthesis of Conjugated Polymers for Organic Solar Cell Applications," *Chemical Reviews* 109 (2009): 5868–5923.

19. J. Roncali, "Synthetic Principles for Bandgap Control in Linear pi-Conjugated Systems," *Chemical Reviews* 97 (1997): 173–205.

20. D. Zhang, H. H. Cho, J. H. Yum, M. Mensi, and K. Sivula, "An Organic Semiconductor Photoelectrochemical Tandem Cell for Solar Water Splitting," *Advanced Energy Materials* 12, no. 42 (2022): 2202363, https://doi.org/10.1002/aenm.202202363.

21. J. Kosco, S. Gonzalez-Carrero, C. T. Howells, et al., "Generation of Long-Lived Charges in Organic Semiconductor Heterojunction Nanoparticles for efficient Photocatalytic Hydrogen Evolution," *Nature Energy* 7 (2022): 340–351.

22. E. M. Speller, A. J. Clarke, J. Luke, et al., "From Fullerene Acceptors to Non-Fullerene Acceptors: Prospects and Challenges in the

Stability of Organic Solar Cells," *Journal of Materials Chemistry A* 7 (2019): 23361–23377.

23. Y. Ma, X. Wang, Y. Jia, X. Chen, H. Han, and C. Li, "Titanium Dioxide-Based Nanomaterials for Photocatalytic Fuel Generations," *Chemical Reviews* 114 (2014): 9987–10043.

24. Y. Xiang, X. Wang, X. Zhang, et al., "Highly Efficient Photocatalytic Cr(VI) Reduction by Lead Molybdate Wrapped with D-A Conjugated Polymer under Visible Light," *Journal of Materials Chemistry A* 6 (2017): 153–159.

25. A. García-Eguizábal, M. Gomez Mendoza, M. Barawi, et al., "Nanostructuration Effect of Carbon – Based Phenylene Vinylene Conjugated Porous Polymers on TiO_2 Hybrid Materials for Artificial Photosynthesis," *Small Structures* 5, no. 3 (2024): 2300410, https://doi.org/10.1002/sstr.202300410.

26. B. Zhang, Z. Genene, J. Wang, et al., "Facile Synthesis of Organic–Inorganic Hybrid Heterojunctions of Glycolated Conjugated Polymer-TiO_2–X for Efficient Photocatalytic Hydrogen Evolution," *Small* 20, no. 43 (2024): 2402649, https://doi.org/10.1002/smll.202402649.

27. J. Warnan, J. Willkomm, J. N. Ng, et al., "Solar H_2 Evolution in Water with Modified Diketopyrrolopyrrole Dyes Immobilised on Molecular Co and Ni Catalyst–TiO_2 hybrids," *Chemical Science* 8 (2017): 3070–3079.

28. L. Yang, Y. Yu, J. Zhang, et al., "In-Situ Fabrication of Diketopyrrolopyrrole-Carbazole-Based Conjugated Polymer/TiO_2 Heterojunction for Enhanced Visible Light Photocatalysis," *Applied Surface Science* 434 (2018): 796–805.

29. C. B. Nielsen, M. Turbiez, and I. McCulloch, "Recent Advances in the Development of Semiconducting DPP-Containing Polymers for Transistor Applications," *Advanced Materials* 25 (2013): 1859–1880.

30. S. Qu and H. Tian, "Diketopyrrolopyrrole (DPP)-Based Materials for Organic Photovoltaics," *Chemical Communications* 48 (2012): 3039–3051.

31. G. Krauss, F. Meichsner, A. Hochgesang, et al., "Polydiketopyrrolopyrroles Carrying Ethylene Glycol Substituents as Efficient Mixed Ion-Electron Conductors for Biocompatible Organic Electrochemical Transistors," *Advanced Functional Materials* 31, no. 20 (2021): 2010048, https://doi.org/10.1002/adfm.202010048.

32. J. Kosco, S. Gonzalez-Carrero, C. T. Howells, et al., "Oligoethylene Glycol Side Chains Increase Charge Generation in Organic Semiconductor Nanoparticles for Enhanced Photocatalytic Hydrogen Evolution," *Advanced Materials* 34, no. 22 (2022): 2105007, https://doi.org/10.1002/adma.202105007.

33. C. Cendra, A. Giovannitti, A. Savva, et al., "Role of the Anion on the Transport and Structure of Organic Mixed Conductors," *Advanced Functional Materials* 29, no. 5 (2019): 1807034, https://doi.org/10.1002/adfm.201807034.

34. A. Giovannitti, D. T. Sbircea, S. Inal, et al., "Controlling the Mode of Operation of Organic Transistors Through Side-Chain Engineering," *Proceedings of the National Academy of Sciences of the United States of America* 113 (2016): 12017–12022.

35. Z. Hu, Z. Wang, X. Zhang, et al., "Conjugated Polymers with Oligoethylene Glycol Side Chains for Improved Photocatalytic Hydrogen Evolution," *iScience* 13 (2019): 33–42.

36. R. J. Lyons, Y. Yang, E. McQueen, et al., "Polymer Photocatalysts with Side Chain Induced Planarity for Increased Activity for Sacrificial Hydrogen Production from Water," *Advanced Energy Materials* 14, no. 12 (2024): 2303680, https://doi.org/10.1002/aenm.202303680.

37. C. J. Mueller, C. R. Singh, M. Fried, S. Huettner, and M. Thelakkat, "High Bulk Electron Mobility Diketopyrrolopyrrole Copolymers with Perfluorothiophene," *Advanced Functional Materials* 25 (2015): 2725–2736.

38. R. Wawrzinek, X. Zhou, M. Ullah, E. B. Namdas, and S. C. Lo, "Aggregates of Diketopyrrolopyrrole Dimers in Solution," *Dyes and Pigments* 136 (2017): 678–685.

39. B. W. H. Saes, M. M. Wienk, and R. A. J. Janssen, "The Effect of α-Branched Side Chains on the Structural and Opto-Electronic Properties of Poly(Diketopyrrolopyrrole-alt-Terthiophene)," *Chemistry A European Journal* 26 (2020): 14221–14228.

40. E. Q. Guo, P. H. Ren, Y. L. Zhang, H. C. Zhang, and W. J. Yang, "Diphenylamine End-Capped 1,4-Diketo-3,6-Diphenylpyrrolo[3,4-c] Pyrrole (DPP) Derivatives With Large Two-Photon Absorption Cross-Sections and Strong Two-Photon Excitation Red Fluorescence," *Chemical Communications* (2009): 5859–5861.

41. Y. Qu, Y. Wu, Y. Gao, S. Qu, L. Yang, and J. Hua, "Diketopyrrolopyrrole-Based Fluorescent Conjugated Polymer for Application of Sensing Fluoride Ion and Bioimaging," *Sensors and Actuators B: Chemical* 197 (2014): 13–19.

42. C. J. Mueller, E. Gann, C. R. McNeill, and M. Thelakkat, "Influence of Fluorination in π-Extended Backbone Polydiketopyrrolopyrroles on Charge Carrier Mobility and Depth-Dependent Molecular Alignment," *Journal of Materials Chemistry C* 3 (2015): 8916–8925.

43. B. W. H. Saes, M. Lutz, M. M. Wienk, S. C. J. Meskers, and R. A. J. Janssen, "Tuning the Optical Characteristics of Diketopyrrolopyrrole Molecules in the Solid State by Alkyl Side Chains," *Journal of Physical Chemistry C* 124 (2020): 25229–25238.

44. M. Grzybowski, E. Glodkowska-Mrowka, G. Clermont, M. Blanchard-Desce, and D. T. Gryko, "Synthesis and Optical Properties of Water-Soluble Diketopyrrolopyrroles," *Chemistry of Heterocyclic Compounds* 53 (2017): 72–77.

45. K. Gräf, M. A. Rahim, S. Das, and M. Thelakkat, "Complementary Co-Sensitization of an Aggregating Squaraine Dye in Solid-State Dye-Sensitized Solar Cells," *Dyes and Pigments* 99 (2013): 1101–1106.

46. J. L. Bredas, "*Materials Horizons*," 1 (2013): 17–19.

47. L. Liu, W. Jiang, X. Song, Q. Duan, and E. Zhu, "A Novel Strategy of Lock-in Effect Between Conjugated Polymer and TiO_2 Towards Dramatic Enhancement of Photocatalytic Activity Under Visible Light," *Scientific Reports* 10, no. 1 (2020): 6513, https://doi.org/10.1038/s41598-020-63623-2.

48. K. Wenderich and G. Mul, "Methods, Mechanism, and Applications of Photodeposition in Photocatalysis: A Review," *Chemical Reviews* 116 (2016): 14587–14619.

49. B. Chen, X. Wang, W. Dong, et al., "Enhanced Light-Driven Hydrogen-Production Activity Induced by Accelerated Interfacial Charge Transfer in Donor–Acceptor Conjugated Polymers/TiO_2 Hybrid," *Chemistry A European Journal* 25 (2019): 3362–3368.

50. H. J. Hou, X. H. Zhang, D. K. Huang, et al., "Conjugated Microporous Poly(Benzothiadiazole)/TiO_2 Heterojunction for Visible-Light-Driven H_2 Production and Pollutant Removal," *Applied Catalysis B: Environmental* 203 (2017): 563–571.

Supporting Information

Additional supporting information can be found online in the Supporting Information section.